

Inductive source induced polarization

David Marchant, Eldad Haber and Douglas W. Oldenburg

Department of Earth and Ocean Sciences, University of British Columbia, Vancouver, BC V6T 1Z4, Canada. E-mail: dmarchant@eos.ubc.ca

Accepted 2012 October 22. Received 2012 September 28; in original form 2012 January 17

SUMMARY

Induced polarization (IP) surveys are commonly performed to map the distribution of electrical chargeability that is a diagnostic physical property in mineral exploration and in many environmental problems. Although these surveys have been successful in the past, the galvanic sources required for traditional IP and magnetic IP (MIP) surveys prevent them from being applied in some geological settings. We develop a new methodology for processing frequency domain EM data to identify the presence of IP effects in observations of the magnetic fields arising from an inductive source. The method makes use of the asymptotic behaviour of the secondary magnetic fields at low frequency. A new quantity, referred to as the ISIP datum, is defined so that it equals zero at low frequencies for any frequency-independent (non-chargeable) conductivity distribution. Thus, any non-zero response in the ISIP data indicates the presence of chargeable material. Numerical simulations demonstrate that the method can be applied even in complicated geological situations. A 3-D inversion algorithm is developed to recover the chargeability from the ISIP data and the inversion is demonstrated on synthetic examples.

Key words: Inverse theory; Electrical properties; Electromagnetic theory.

1 INTRODUCTION

The presence of polarizable material in the ground is an excellent proxy for the distribution of metallic minerals and hence IP surveys are routinely used for mineral exploration (Fink *et al.* 1990). Recent studies have also applied the observation of IP effects to hydrocarbon exploration (Davydycheva *et al.* 2006; Veeken *et al.* 2012), hydrogeological mapping (Slater & Glaser 2003; Hördt *et al.* 2007), and numerous other environmental and engineering applications. The causes of electric polarization, or equivalently chargeability, are varied but regardless of the cause, a chargeable material will have a complex, frequency-dependent conductivity.

Traditionally, measurements of chargeability are carried out using the IP technique (Seigel 1959). This purely galvanic technique injects current into the ground through a pair of transmitter electrodes and then measures the voltage decay across another set of electrodes after the current has been interrupted. An excellent summary of the historical development of the IP method was given by Seigel *et al.* (2007). The method has a proven track record in mineral exploration and is widely considered the geophysical method of choice when looking for porphyry copper deposits (Fink *et al.* 1990). These data are now commonly inverted to recover 2-D or 3-D models of the chargeability distribution in the ground (Oldenburg & Li 1994; Li & Oldenburg 2000).

Despite the method's success, its application is not always practical. The time and cost required to survey large areas can often be prohibitively large. Some geological settings can also cause traditional IP to fail. For example, the method struggles in regions where

highly conductive or highly resistive overburden exists. In areas of high conductivity, the overburden essentially short-circuits the electrode pairs. When high resistivity is present it becomes difficult to inject enough current into the ground to excite the polarizable body.

Seigel (1974) proposed an alternate method for mapping chargeability that addresses some of these shortcomings. The method was called the magnetic induced polarization (MIP) technique. In this technique, current is again injected into the ground across two transmit electrodes, but observations of the secondary magnetic field are used rather than electrical potentials. This eliminates the time consuming requirement of placing receiver electrodes, and provides improved performance when operating where highly conductive overburden exists. A 3-D inversion technique for MIP data was developed by Chen & Oldenburg (2003).

The MIP method requires that current be injected into the ground and thus it still suffers in areas covered by highly resistive overburdens. To get away from this requirement, one must move to a purely inductive method. The idea of inductive induced electrical polarization was examined by Hohmann *et al.* (1970). They considered frequency-domain measurements acquired above a 1-D, chargeable 2-layer Earth as well as field data collected above known conventional IP responses. They considered only the magnitude of the magnetic field as data. In the synthetic tests, though the presence of a chargeable layer did affect the data, the changes were very small. Although such changes could be explained in terms of chargeable material it seemed that a heterogeneous model with frequency-independent conductivity could provide another possible explanation.

The majority of literature on the effects of chargeability on inductive EM focuses on concentric and in-loop TEM surveys where the presence of negative responses have long been observed. Morrison *et al.* (1969) showed that these responses could be explained by 1-D layered structures exhibiting extreme chargeabilities. Weidelt (1982) went further and theoretically showed that coincident loop responses must be of the same sign in the presence of frequency-independent conductivity and magnetic permeability. Thus, sign reversals in these data must be associated with the presence of polarization effects (Smith & West 1988).

Numerous works have been published on the explanation and interpretation of these effects, whereas very little has been published on the effects of chargeability on frequency domain surveys, or on surveys with geometries other than centre loop. Some exceptions are Gasperikova & Morrison (2001), who looked at IP effects in MT data, and Hoheisel *et al.* (2004) who studied IP effects in LOTEM data.

In this work, we propose a new data collection, processing and inversion methodology to map the distribution of chargeability using inductive sources and observations of magnetic fields in the frequency domain. We exploit the asymptotic behaviour of the magnetic fields at low frequencies to identify the presence of an IP response, and develop an inversion scheme to recover the 3-D distribution of chargeability.

2 A MATHEMATICAL MODEL FOR INDUCTIVE SOURCE IP

In this section, we examine the behaviour of Maxwell's equations at low frequency. In particular, we are interested in how the presence of a chargeable material will affect the resulting magnetic fields.

Maxwell's equations in the frequency domain are

$$\nabla \times \mathbf{E} - i\omega\mu\mathbf{H} = 0 \quad (1)$$

$$\nabla \times \mathbf{H} - \sigma\mathbf{E} = \mathbf{s}. \quad (2)$$

Here, \mathbf{E} and \mathbf{H} are the electric and magnetic fields, σ is the conductivity and μ the magnetic susceptibility. Define \mathbf{H} such that $\mathbf{H} = \mathbf{H}_0 + \mathbf{H}^s$ and $\nabla \times \mathbf{H}_0 = \mathbf{s}$. Here, \mathbf{H}_0 is the magnetic field generated by the loop at zero frequency, which can be calculated using the Biot–Savart law. We can rewrite eq. (1) in terms of \mathbf{H}^s as

$$\nabla \times \mathbf{E} - i\omega\mu\mathbf{H}^s = i\omega\mu\mathbf{H}_0 \quad (3a)$$

$$\nabla \times \mathbf{H}^s - \sigma\mathbf{E} = 0. \quad (3b)$$

Eliminating \mathbf{E} from the system yields an equation for \mathbf{H}^s

$$\nabla \times \rho \nabla \times \mathbf{H}^s - i\omega\mu\mathbf{H}^s = i\omega\mu\mathbf{H}_0, \quad (4)$$

where ρ is the resistivity, $\rho = \frac{1}{\sigma}$. This equation represents the forward problem for magnetic fields arising from an inductive source.

Now, assume a frequency-independent (non-chargeable) resistivity distribution ρ . We can compute the derivatives of \mathbf{H}^s with respect to ω by differentiating eq. (4). Differentiating once we obtain

$$\nabla \times \rho \nabla \times \frac{\partial \mathbf{H}^s}{\partial \omega} - i\omega\mu \frac{\partial \mathbf{H}^s}{\partial \omega} = i\mu (\mathbf{H}_0 + \mathbf{H}^s). \quad (5)$$

Eq. (5) is a partial differential equation for $\frac{\partial \mathbf{H}^s}{\partial \omega}$. It has the same form as the system for \mathbf{H}^s but a different right-hand side. From eq. (5) we see that as $\omega \rightarrow 0$ the derivative $\frac{\partial \mathbf{H}^s}{\partial \omega}$ becomes is purely imaginary,

giving

$$\text{Im} [\mathbf{H}^s(\omega, \rho)] \approx \frac{\partial \mathbf{H}^s}{\partial \omega} \Big|_{\omega=0} \omega \quad (6)$$

or

$$\frac{\text{Im} [\mathbf{H}^s(\omega, \rho)]}{\omega} \approx \frac{\partial \mathbf{H}^s}{\partial \omega} \Big|_{\omega=0} \approx \text{const.} \quad (7)$$

2.1 Inductive source IP

So far we have shown that the behaviour of the imaginary part of the magnetic field can be easily predicted at low frequencies when no chargeable material is present. This property can be used to detect chargeability.

Consider the magnetic response of a non-chargeable Earth to forcing from an inductive source operating at two closely spaced, low frequencies ω_1 and ω_2 . If the frequencies are sufficiently low then the skin-depth is very large compared to the geometric decay of the source fields and the measured response is sensitive to the same volume of Earth. From eq. (7) we can say that

$$\frac{\text{Im} [\mathbf{H}^s(\omega_2)]}{\omega_2} - \frac{\text{Im} [\mathbf{H}^s(\omega_1)]}{\omega_1} \approx 0. \quad (8)$$

This observation motivates us to introduce a new quantity d^{ISIP} which we define as the inductive source IP (ISIP) data

$$d^{\text{ISIP}} = \text{Im} [\mathbf{H}^s(\omega_2)] - \frac{\omega_2}{\omega_1} \text{Im} [\mathbf{H}^s(\omega_1)]. \quad (9)$$

A datum is obtained by taking a scaled linear combination of two recorded magnetic fields, thus the ISIP data are secondary signals that are directly related to the chargeable Earth. For any real, non-dispersive resistivity distribution the ISIP data, d^{ISIP} , should approximately equal zero. Non-zero values indicate the presence of chargeable material. This is an important benefit.

It is interesting to note that a similar definition of data was used by Beard & Zhou (1995), Wang *et al.* (2003) to correct downhole data for unwanted noise that arises by a logging tool not being centred in the borehole. These effects, caused by conductivity contrasts located very close to the tool and in the low-induction number regime, varied linearly with frequency and could be largely accounted for by applying what they name a dual frequency approach. In their treatment, they assume that conductivity structures are non-dispersive. From our analysis, if the material near the borehole had a conductivity that was dispersive, then IP signal would still reside in their processed data.

We now demonstrate the effectiveness of the ISIP data in recovering chargeable targets using a few examples.

2.1.1 Synthetic example #1—two blocks in a half-space

We test the sensitivity of the ISIP data to chargeable material by using two synthetic examples. The first test consists of two conductive blocks in a resistive half-space. Both blocks have a resistivity of 1 Ωm and the background has resistivity of 1000 Ωm . One of the blocks is chargeable. In the second test we use the same two blocks but embed them in a more complicated geological background.

The frequency dependence of a material's resistivity is commonly parametrized by the Cole–Cole model (Cole & Cole 1941; Pelton *et al.* 1978)

$$\rho(\omega) = \rho_0 \left[1 - \eta \left(1 - \frac{1}{1 + (i\omega\tau)^c} \right) \right], \quad (10)$$

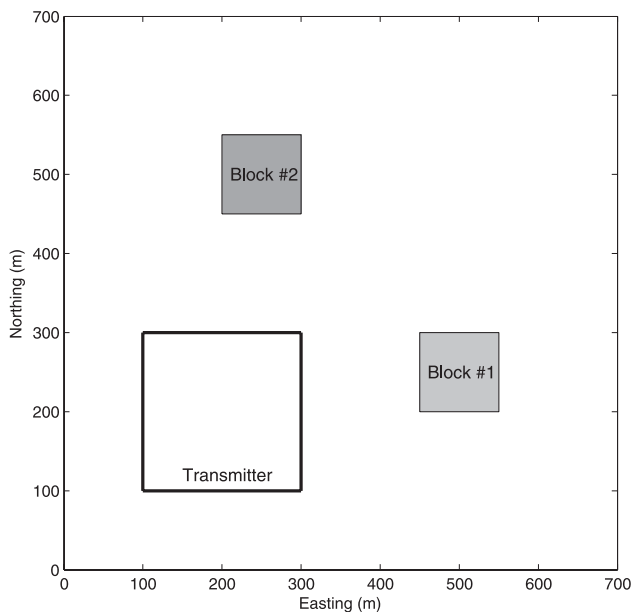


Figure 1. Geometry of the two block model. The tops of the blocks are 125 m below the surface, and they extend to a depth of 225 m. Block #1 is conductive (1 Ωm) but it is not chargeable. Block #2 is conductive and chargeable, with Cole–Cole parameters $\rho_0 = 1 \Omega\text{m}$, $\eta = 0.1$, $\tau = 0.1$ and $c = 0.5$. The background half-space has a resistivity of 1000 Ωm . The dark black line shows the layout of the transmitter wire.

where ρ_0 (Ωm) is the resistivity at zero frequency, η is the chargeability, τ (s) is a time constant and c is the frequency dependence. In this example, the chargeable block is modelled with Cole–Cole parameters $\eta = 0.1$, $\tau = 0.1$ and $c = 0.5$. Although this choice of Cole–Cole parameters is not based on any specific set of measurements, they are reasonable when compared to best fitting models of porphyry deposits from Pelton *et al.* (1978), Wong (1979). The tops of the blocks are buried 125 m below the surface of the half-space. There is a single transmitter that is offset from the two conductive blocks and the magnetic fields are simulated at 1 and 2 Hz (Fig. 1). These parameters result in a change between the two frequencies of $1.0 \times 10^{-2} \Omega\text{m}$ in the real part and $2.4 \times 10^{-4} \Omega\text{m}$ in the imaginary part of the resistivity of the chargeable block.

The resulting magnetic fields, and the calculated ISIP data are shown in Fig. 2. The magnetic fields at the two frequencies are similar in form but have different amplitudes. It is difficult to determine the presence of the blocks from the appearance of the magnetic fields, let alone determine whether either of them are chargeable. Eq. (9) was used to calculate the ISIP data from these magnetic fields. The ISIP data are shown in the third column in Fig. 2. The existence and approximate location of the chargeable block is easily determined from looking at these plots.

2.1.2 Synthetic example #2—two blocks in a complex background

In the second synthetic example the same two blocks were placed in a complicated 3-D background, and buried beneath a very resistive overburden. The resistivity of the background units vary between 10 and 1000 Ωm . The overburden has a resistivity of 10 000 Ωm . Cross-sections through this model are shown in Fig. 3. The resulting magnetic fields, and the calculated ISIP data are shown in Fig. 4. The anomalous ISIP response from the chargeable block is clearly evident and it is very similar to that of the previous example despite

the fact that the chargeable body was buried in a host with a very different conductivity structure.

3 SOURCES OF ERROR

The results in the last section showed that ISIP data can be a direct indicator of polarizable material. The important question pertains to whether or not the ISIP signal is large enough to be measured in field situations. To be useful the ISIP signal must be larger than the ‘noise’. There are two factors to be considered. The first is the intrinsic noise of the instrument; the second is the ‘noise’ inherent in our analysis procedure when our low frequency assumption is violated. We consider each of these in turn.

3.1 Noisy magnetic fields and error propagation

An ISIP datum is a linear combination of two measured data and hence its variance is determined by the accuracy of each measurement. If we assume that the observations of $\text{Im}[\mathbf{H}^s(\omega_1)]$ have a variance of σ_{h_1} , that $\text{Im}[\mathbf{H}^s(\omega_2)]$ has a variance of σ_{h_2} and that errors are uncorrelated then the variance in the resulting ISIP data is

$$\sigma_{\text{ISIP}} = \sqrt{\sigma_{h_2}^2 + \left(\frac{\omega_2}{\omega_1}\sigma_{h_1}\right)^2}. \quad (11)$$

In the case where $\sigma_{h_1} = \sigma_{h_2} = \sigma_h$ this simplifies to

$$\sigma_{\text{ISIP}} = \sqrt{1 + \left(\frac{\omega_2}{\omega_1}\right)^2} \sigma_h. \quad (12)$$

Thus, the variance in the ISIP data will always be larger than the variance in the measurements of the magnetic fields used to calculate the ISIP response. It is important to note that though the magnitude of the variance will only slightly increase for closely spaced frequencies, the magnitude of the ISIP data will be significantly less than the magnitude of the original magnetic fields as a result of eq. (9). This results in an increase in the relative variance of the ISIP data compared to the relative variance in the original magnetic fields.

Using modern SQUID magnetometers, resolutions of 20fT ($1.6 \times 10^{-8} \text{ A m}^{-1}$) have been achieved at 1 Hz (Kawai *et al.* 1999). If we choose instrumentation noise to be $20\text{fT}/\sqrt{\text{Hz}}$ and frequencies of 1 and 2 Hz, then $\sigma_{\text{ISIP}} = 4.3 \times 10^{-8} \text{ A m}^{-1}$.

The magnitude of the ISIP signal is controlled by many factors and is something that will analysed in more detail in future papers. Principally however, it depends upon the size and geometry of the target and its location relative to the transmitter, the geometry of the transmitter and the magnitude of the current, the Cole–Cole (or other complex conductivity description of the target material) and the choice of frequencies. The relationship between most of these parameters and the ISIP data is complicated. The exception is transmitter current; the ISIP data depend linearly on the magnitude of the current.

To illustrate the fact that ISIP data can be large enough to be recorded with current instruments, we continue with the example used in the paper. For a 1A current the maximum ISIP signal in Fig. 4 occurs in the z-component and is $0.35 \times 10^{-8} \text{ A m}^{-1}$. The estimated standard deviation for this datum is $\sigma_{\text{ISIP}} = 4.3 \times 10^{-8} \text{ A m}^{-1}$. In Fig. 5 we show the noisy ISIP that would be measured when the transmitter current is respectively 1, 10 and 50 A. EM transmitters capable of producing currents up to 50 A are commonly available

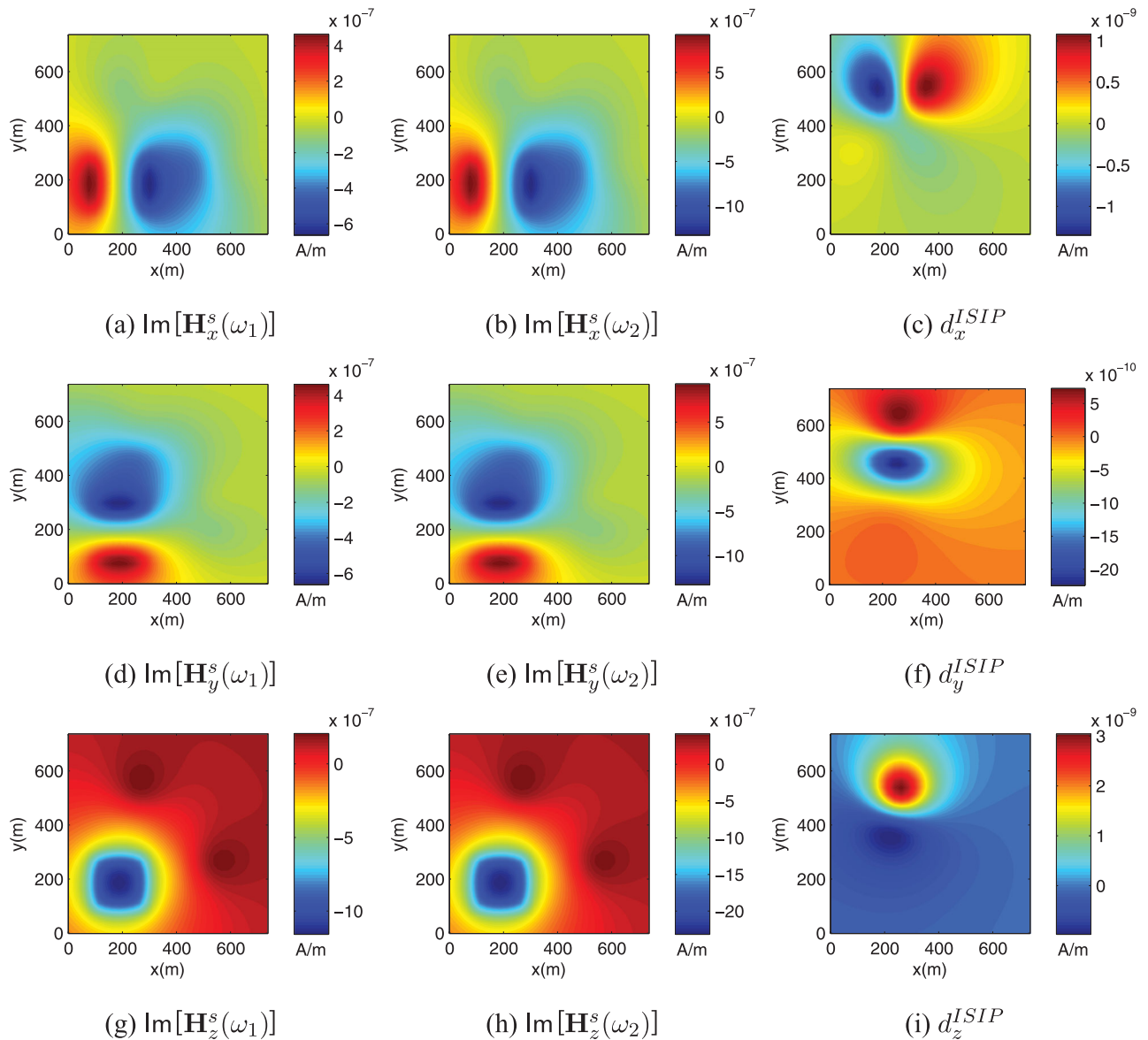


Figure 2. The x , y and z components of the imaginary part of the magnetic fields (A m^{-1}) simulated at 1 and 2 Hz and the calculated ISIP data. The centre of the chargeable block is located at (250 m, 500 m) and the centre of the conductive block is located at (500 m, 250 m).

on the market today. With a 50 A transmitter, and resolving power of $4.3 \times 10^{-8} \text{ A m}^{-1}$ the ISIP response is easily visible in the data (Fig. 5).

This is just an example and it does not represent the best case scenario. Different transmitter and receiver geometries, a shallower target, or a different Cole–Cole model could achieve a higher magnitude response.

3.2 Low frequency assumption

The second area in which ‘noise’ can contaminate our analysis occurs if our low frequency assumptions are violated. Low frequencies are required in this derivation for two reasons. First, though deriving the expressions for the ISIP data, it was assumed that observations of the magnetic fields are made at sufficiently low frequencies that the higher order terms of the expansion of eq. (4) can be dropped. The imaginary portion of the recorded magnetic field then depends linearly upon frequency. The value of the induction number is the

determining factor in the validity of this assumption. As long as the induction number is much less than unity, the ISIP data will be equal to zero unless chargeable material is present. As the value of the induction number increases however, additional sources of signal become apparent in the data. Also, as induction number increases so that the linear dependence on frequency begins to be violated, it may be necessary to restrict the difference between the two frequencies that are used to compute the ISIP data. However, reducing the difference between the two frequencies will also reduce the magnitude of the ISIP signal. The details about this deserve further attention but for now we illustrate that the non-linearity due to inductive effects is not so large that it prevents quality ISIP data to be recorded at relatively high frequencies. We return to the ISIP data for the simple two block model used in the first example, except we compute data using frequencies from 5 to 55 Hz. The resultant data are shown in Fig. 6. ISIP data require measurements of magnetic field at two frequencies. The lower of the two frequencies used are shown in the figure. The higher frequency is 5 per cent larger. In each case,

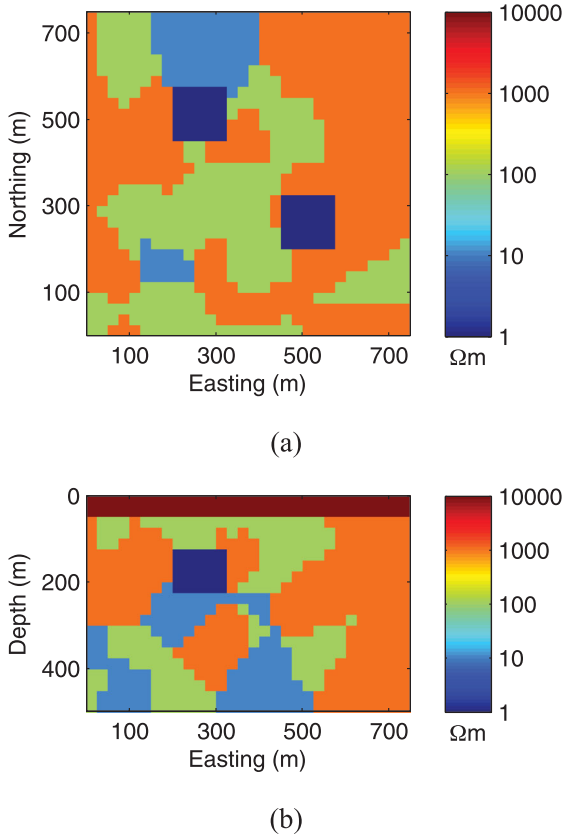


Figure 3. The real part of the complex 3-D resistivity model. The background is not chargeable and the resistivity of the units varies from 10 to 1000 Ωm . The overburden is 50 m thick and has a resistivity of 10 000 Ωm . The two blocks have the same properties as they did in the previous example. (a) Depth slice 150 m below the surface. (b) Slice through the model at 500 m north.

the Cole–Cole model is slightly modified to ensure that the difference in resistivity between the two frequencies remains constant. At low frequencies, the ISIP data are a dipolar response centred over the chargeable block. As the frequencies increase, non-zero signals begin to appear in the ISIP data away from the chargeable block. At these frequencies, starting around 25 Hz, the magnetic fields no longer vary linearly with frequency.

4 DISCRETIZATION OF THE ISIP FORWARD MODELLING

In this section, we discuss how to obtain a discrete systems of equations for the ISIP data. Since the ISIP data are derived from the magnetic field we briefly discuss the discretization of Maxwell’s equations. We then linearise the problem to obtain a discrete linear inverse problem for the distribution of chargeable material given the ISIP data.

4.1 Discretization of Maxwell’s equations

We consider the system for \mathbf{H}^s given ρ (eq. 4). The system has a non-trivial null space (the gradient of scalar functions) when $\omega \rightarrow 0$ and therefore must be stabilized. To stabilize the system at very low frequency we use the source condition $\nabla \cdot \mu \mathbf{H}^s = 0$ and,

assuming μ is constant, we add $\nabla \rho \nabla \cdot \mathbf{H}^s$ to Maxwell’s equations (4) to obtain

$$\nabla \times \rho \nabla \times \mathbf{H}^s - \nabla \rho \nabla \cdot \mathbf{H}^s - i\omega \mu \mathbf{H}^s = i\omega \mu \mathbf{H}_0. \quad (13)$$

This guaranties a solution of the system even for $\omega = 0$ (Haber & Ascher 2001). For boundary conditions we use $\mathbf{n} \times \mathbf{H}^s = 0$. For numerical evaluation, we discretize the system on an orthogonal, staggered grid and use a finite volume approach (Yee 1966) with material averaging of resistivities (Haber & Ascher 2001).

\mathbf{H}^s is placed on cell edges and ρ is defined at the cell centres. The discrete equation is

$$\begin{aligned} & [\mathbf{curl}^\top \text{diag}(\mathbf{A}_c^e \rho) \mathbf{curl} - \mathbf{grad} \text{diag}(\mathbf{A}_c^n \rho) \mathbf{grad}^\top - i\omega \mu \mathbf{I}] \mathbf{H}^s \\ & = i\omega \mu \mathbf{H}_0, \end{aligned} \quad (14)$$

where \mathbf{curl} and \mathbf{grad} are discrete forms of the curl and gradient operators, obtained by short differences on staggered grids and \mathbf{A}_c^e and \mathbf{A}_c^n are averaging matrices from cell to edges and nodes respectively. The system is solved for \mathbf{H}^s using a direct solver (Amestoy *et al.* 2006).

4.2 Linearization of inductive source IP equations

To invert for chargeable material we need to connect the ISIP data to changes in the resistivity with frequency. Since this change is small we use simple linearization. This is similar to the DCIP case where the IP effect is obtained by linearizing the DC equations (Oldenburg & Li 1994).

Chargeability causes small perturbations in resistivity as a function of frequency. Let ρ_1 and ρ_2 be the resistivities that would be observed at frequencies ω_1 and ω_2 . Since the frequencies ω_1 and ω_2 are closely spaced, the resistivity that would be observed at ω_2 is approximately equal to the resistivity at ω_1 plus a small perturbation, or $\rho_2 \approx \rho_1 + \delta\rho$. Expanding the magnetic field using the first-order Taylor’s expansion around $\rho = \rho_1$ we obtain

$$\mathbf{H}^s(\omega_2, \rho_2) \approx \mathbf{H}^s(\omega_2, \rho_1) + \frac{\partial \mathbf{H}^s}{\partial \rho}(\omega_2, \rho_1) \delta\rho. \quad (15)$$

Define the complex sensitivity matrix \mathbf{J} to be

$$\mathbf{J} = \mathbf{Q} \frac{\partial \mathbf{H}^s}{\partial \rho}(\omega_2, \rho_1), \quad (16)$$

where \mathbf{Q} is a projection matrix that projects the magnetic field \mathbf{H}^s to the receiver locations. The (i, j) element of \mathbf{J} contains how the i th observation of \mathbf{H}^s will be affected by a small perturbation in resistivity in the j th cell. Using the result from eq. (7) we can say that

$$\text{Im}[\mathbf{QH}^s(\omega_2, \rho_1)] \approx \frac{\omega_2}{\omega_1} \text{Im}[\mathbf{QH}^s(\omega_1, \rho_1)]. \quad (17)$$

Combining this expression with eq. (15) yields

$$\text{Im}[\mathbf{QH}^s(\omega_2, \rho_2)] \approx \frac{\omega_2}{\omega_1} \text{Im}[\mathbf{QH}^s(\omega_1, \rho_1)] + \text{Im}(\mathbf{J}\delta\rho). \quad (18)$$

Then, using the definition of the ISIP data (eq. 9), projecting to the receiver locations, we obtain

$$d^{\text{ISIP}} = \text{Im}(\mathbf{J}\delta\rho) = \mathbf{J}_{\text{Re}} \delta\rho_{\text{Im}} + \mathbf{J}_{\text{Im}} \delta\rho_{\text{Re}}, \quad (19)$$

where we use the notation $(\cdot)_{\text{Re}}$ and $(\cdot)_{\text{Im}}$ to denote the real and imaginary components of (\cdot) .

This is a coupled system for $[\delta\rho_{\text{Re}}, \delta\rho_{\text{Im}}]$ given the ISIP data. Fortunately, the system can be decoupled when working at low

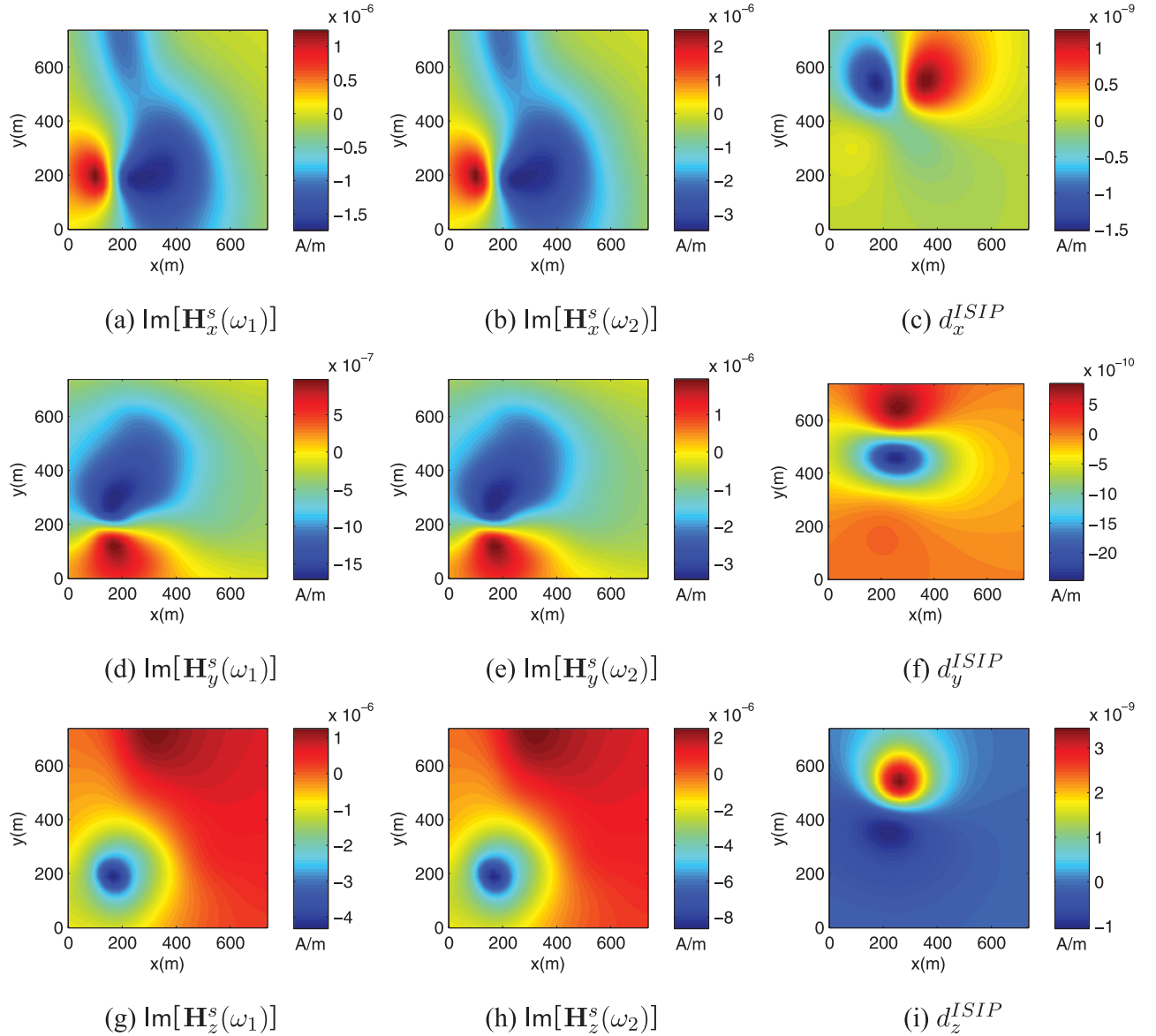


Figure 4. The x , y and z components of the imaginary part of the magnetic fields (A m^{-1}) simulated at 1 and 2 Hz and the calculated ISIP data above the synthetic model shown in Fig. 3. Despite the complicated 3-D conductivity distribution, the ISIP data still reflects the location of the chargeable body.

frequencies. To see that we analyse the sensitivity matrix obtained around a real resistivity value ρ and low frequency ω .

Differentiating (14) with respect to ρ we obtain

$$\begin{aligned} & [\mathbf{curl}^\top \text{diag}(\mathbf{A}_c^e \rho) \mathbf{curl} - \mathbf{grad} \text{diag}(\mathbf{A}_c^n \rho) \mathbf{grad}^\top - i\omega\mu\mathbf{I}] \frac{\partial \mathbf{H}^s}{\partial \rho} \\ & + [\mathbf{curl}^\top \text{diag}(\mathbf{curl} \mathbf{H}^s) \mathbf{A}_c^e - \mathbf{grad} \text{diag}(\mathbf{grad}^\top \mathbf{H}^s) \mathbf{A}_c^n] = 0 \end{aligned} \quad (20)$$

and therefore, the sensitivity matrix is

$$\begin{aligned} \mathbf{J} = & - [\mathbf{curl}^\top \text{diag}(\mathbf{A}_c^e \rho) \mathbf{curl} - \mathbf{grad} \text{diag}(\mathbf{A}_c^n \rho) \mathbf{grad}^\top - i\omega\mu\mathbf{I}]^{-1} \\ & \times [\mathbf{curl}^\top \text{diag}(\mathbf{curl} \mathbf{H}^s) \mathbf{A}_c^e - \mathbf{grad} \text{diag}(\mathbf{grad}^\top \mathbf{H}^s) \mathbf{A}_c^n]. \end{aligned} \quad (21)$$

Let us examine the sensitivity matrix for low frequencies. The EM forward modelling matrix is

$$\mathbf{A}(\rho) = \mathbf{curl}^\top \text{diag}(\mathbf{A}_c^e \rho) \mathbf{curl} - \mathbf{grad} \text{diag}(\mathbf{A}_c^n \rho) \mathbf{grad}^\top - i\omega\mu\mathbf{I}. \quad (22)$$

The discretization of the differential terms are of order $h^{-2}\rho$ whereas the last term is of order $\omega\mu$ where h is the length of one edge of the smallest cells in the mesh. If $\omega \ll h^{-2}\rho\mu^{-1}$ then the term involved with ω can be neglected, and therefore, for low frequencies we have $\mathbf{A}(\rho) \approx \mathbf{A}(\rho)_{\text{Re}}$.

The second part in the sensitivity involves the differential operators and \mathbf{H}^s . As we have seen previously, in eq. (6), \mathbf{H}^s is dominated by its imaginary part at low frequencies. These two observations imply that $\|\mathbf{J}_{\text{Re}}\| \ll \|\mathbf{J}_{\text{Im}}\|$.

Using the asymptotic properties of \mathbf{J} it is possible to simplify the system (19). As \mathbf{J}_{Re} is very small, the term $\mathbf{J}_{\text{Re}}\delta\rho_{\text{Im}}$ can be dropped

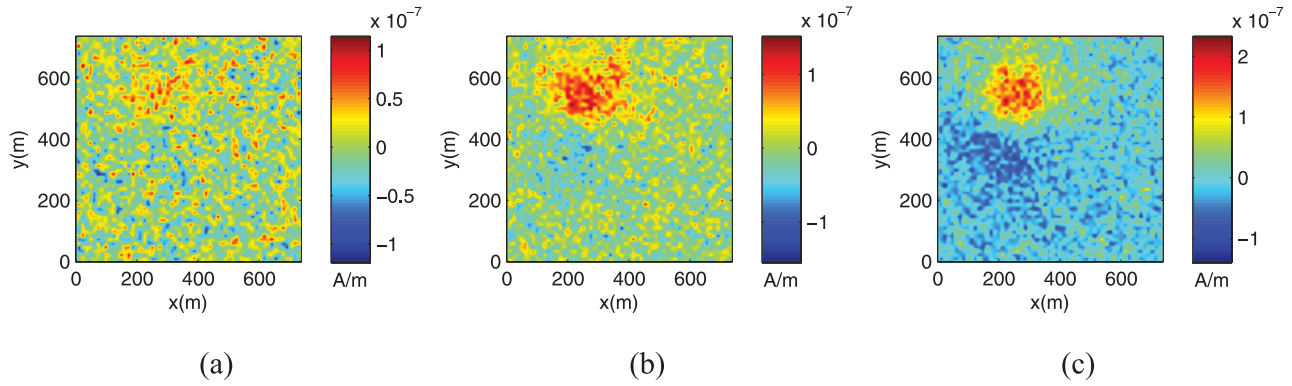


Figure 5. The vertical component of the ISIP data (A m^{-1}) calculated from magnetic fields that had been contaminated with random gaussian noise with a standard deviation of $1.6 \times 10^{-8} \text{ A m}^{-1}$ and a variable transmitter current. (a) 10-A transmitter current (b) 30-A transmitter current (c) 50-A transmitter current

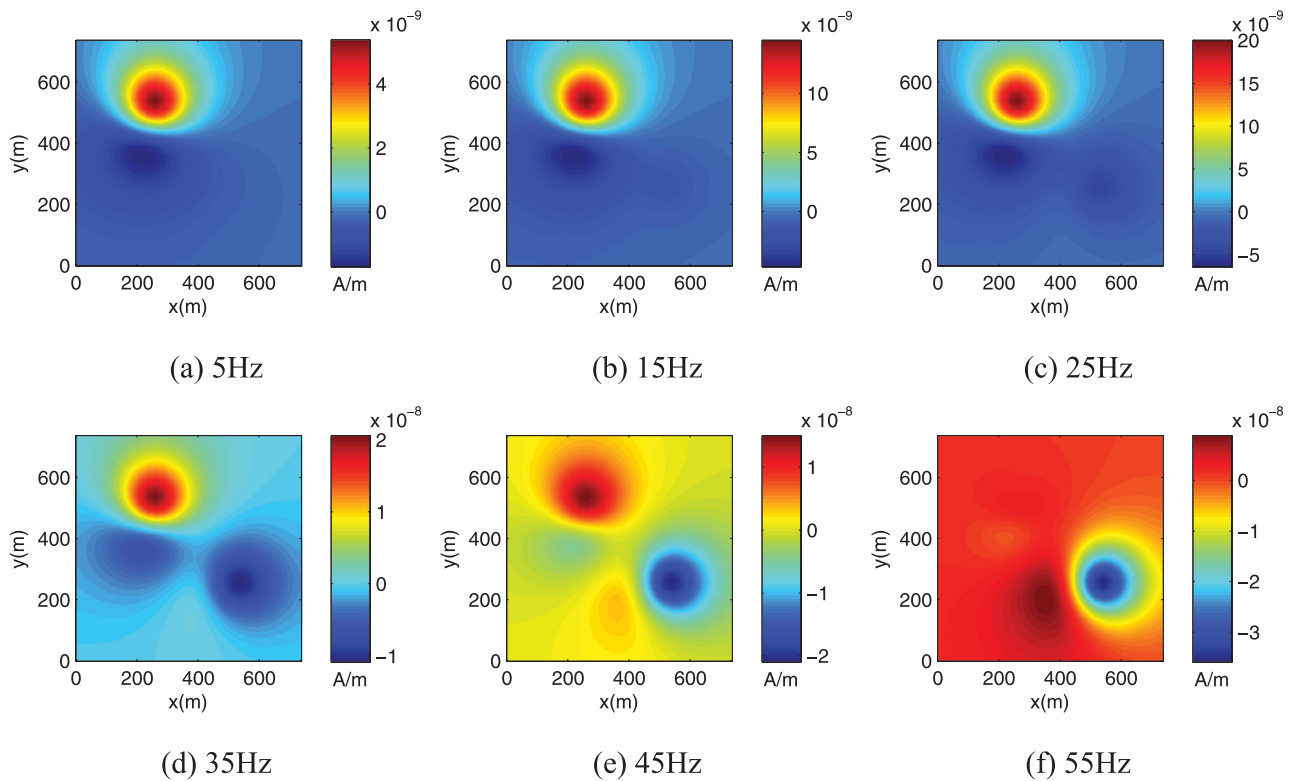


Figure 6. Vertical component of ISIP data for the simple two block model calculated for pairs of frequencies of increasing magnitude. The lower frequency is shown in the figure. The second frequency is 5 per cent higher.

from eq. (19) and we obtain a linear relationship between the ISIP data and $\delta\rho_{\text{Re}}$

$$d^{\text{ISIP}} \simeq \mathbf{J}_{\text{Im}} \delta\rho_{\text{Re}}. \quad (23)$$

5 SOLVING THE LINEAR INVERSE PROBLEM

Recovering $\delta\rho_{\text{Re}}$ using the approximation in eq. (23) is a simple linear inverse problem that can be solved using various techniques. Before inverting the ISIP data for $\delta\rho_{\text{Re}}$, \mathbf{J}_{Re} must be approximated, requiring estimates of ρ (the zero-frequency resistivity structure) and \mathbf{H}^s (the secondary magnetic fields arising from ρ). The esti-

ated resistivity could be obtained by performing a 3-D inversion of data at one of the two frequencies, or it could be generated in some other way.

It is important to note that the ISIP data are sensitive to the change in resistivity between the two frequencies being used, and not to the chargeability parameter used in common dispersion models. The model that results from inverting ISIP data maps the distribution of material that exhibits a change in resistivity between the two frequencies used. In the simple case of materials exhibiting dispersion that can be represented by a Debye model ($c = 1$ in eq. 10), this change will be proportional to the chargeability, η . In materials with other frequency dependencies, the relationship is not so simple. The presence of a non-zero $\delta\rho_{\text{Re}}$ directly indicates a non-zero chargeability, however a zero $\delta\rho_{\text{Re}}$ does not necessarily imply that

the material is not chargeable. It only tells us that the dispersion of the material is such that there is no measurable $\delta\rho_{Re}$ between the frequencies used.

5.1 Inversion methodology

Our inversion methodology is based upon that described in Li & Oldenburg (2000). The solution to the inverse problem is the model \mathbf{m} that solves the optimisation problem

$$\begin{aligned} \min \quad & \phi = \phi_d(\mathbf{m}) + \beta\phi_m(\mathbf{m}) \\ \text{s.t.} \quad & 0 \leq \mathbf{m}. \end{aligned} \quad (24)$$

In this equation, ϕ_d is a measure of the data misfit, ϕ_m is a user defined model objective function and β is regularization or trade-off parameter. We use the sum of the squares to measure data misfit

$$\phi_d = \|\mathbf{W}_d(\mathbf{G}\mathbf{m} - \mathbf{d}^{\text{obs}})\|_2^2 = \sum_{i=1}^N \left(\frac{\mathbf{d}_i^{\text{pred}} - \mathbf{d}_i^{\text{obs}}}{\epsilon_i} \right)^2, \quad (25)$$

where N is the number of observed data and \mathbf{W}_d is a diagonal data weighting matrix which contains the reciprocal of the estimated uncertainty of each datum (ϵ_i) on the main diagonal.

The model objective function, ϕ_m , is a measure of amount of structure in the model and, upon minimization, will generate a smooth model this is close to a reference model \mathbf{m}_{ref} . We define ϕ_m as

$$\begin{aligned} \phi_m = & \alpha_s \|\mathbf{W}_s(\mathbf{m} - \mathbf{m}_{\text{ref}})\|_2^2 + \alpha_x \|\mathbf{W}_x(\mathbf{m} - \mathbf{m}_{\text{ref}})\|_2^2 \\ & + \alpha_y \|\mathbf{W}_y(\mathbf{m} - \mathbf{m}_{\text{ref}})\|_2^2 + \alpha_z \|\mathbf{W}_z(\mathbf{m} - \mathbf{m}_{\text{ref}})\|_2^2, \end{aligned} \quad (26)$$

where \mathbf{W}_s is a diagonal matrix, and \mathbf{W}_x , \mathbf{W}_y and \mathbf{W}_z are discrete approximations of the first derivative operator in the x , y and z directions, respectively. The α 's are weighting parameters that balance the relative importance of producing small or smooth models.

The ISIP data equations are linear but the inverse problem is non-linear because we impose bound constraints on \mathbf{m} to ensure reasonable valued results. The constrained optimisation problem is solved using the Projected Newton method detailed in Kelley (1999). At the $(n+1)^{\text{th}}$ iteration, this method requires the solution to

$$\mathbf{R}\delta\mathbf{m} = -\mathbf{G}^T \mathbf{W}_d^T \mathbf{W}_d (\mathbf{d}^{\text{obs}} - \mathbf{d}^n) - \beta \mathbf{W}^T \mathbf{W} (\mathbf{m}^n - \mathbf{m}_{\text{ref}}), \quad (27)$$

where \mathbf{m}^n is model produced at the n th iteration, \mathbf{d}^n are the data predicted by \mathbf{m}^n , \mathbf{W} is the regularization matrix and \mathbf{R} is the reduced Hessian.

We solve eq. (27) using a pre-conditioned conjugate gradient algorithm. This approach allows $\delta\mathbf{m}$ to be obtained with only the multiplication of \mathbf{R} onto a vector. Once the search direction $\delta\mathbf{m}$ has been identified, the new model is given by $\mathbf{m}^{n+1} = \text{Proj}(\mathbf{m}^n + \gamma\delta\mathbf{m})$, where γ ($0 < \gamma \leq 1$) is chosen by a simple backtracking line search such that \mathbf{m}^{n+1} reduces the objective function. Proj is a projection operator that projects the updated model back to feasible model space.

The regularization parameter is chosen using a cooling schedule. β is initially chosen to the very large so that $\beta\phi_m$ dominates the objective function. When the \mathbf{m} that minimizes eq. (24) is identified, β is decreased by a constant factor. This continues until the desired level of data misfit is achieved.

5.2 Inversion of synthetic ISIP data

The response of the model shown in Fig. 3 was calculated for a survey consisting of 25 transmitters laid out in a 5×5 grid. Each

transmitter was a square loop, 200 m on a side. 169 receivers (13×13 grid) recorded the three components of the magnetic fields at 1 and 2 Hz. The survey was simulated by solving eq. (14) at each of the two frequencies. The resulting data were then contaminated with random Gaussian noise with a standard deviation of 5.3×10^{-10} A m⁻¹ (the noise level you could expect from a receiver with 1.6×10^{-8} A m⁻¹ resolution while transmitting 30 A). Three components of ISIP data were then calculated from the simulated noisy magnetic fields using eq. (9). This resulted in 12 675 unique data. Non-chargeable half-spaces were used for both the initial and reference models in the subsequent inversions. In this example, the real part of the true background resistivity model was used when calculating the sensitivities.

A plan view and cross-section of the true and recovered $\delta\rho_{Re}$ models are shown in Fig. 7. The depth and horizontal extents of the chargeable material are well located. As usual, with such inversions, there is some extension of the chargeability away from the boundaries of the true block and also the amplitude of the recovered chargeability is lower than the true value. This is a result of the smallness and smoothness terms used to regularize the inversion (Oldenburg & Li 2005). Overall, the inversion has been successful in locating the chargeable material.

5.2.1 Importance of background conductivity model

Calculation of the sensitivities, which form a central role in the inversion of the ISIP data, require knowledge of the background resistivity. In the previous example, the real part of the true resistivity was used. In reality however, this quantity is not known, and an estimate of the resistivity structure must be used. Depending on the method used to generate the estimate, the model may not be a good representation of the true resistivities in the area of interest.

To test the importance of the background resistivity model, two additional inversions were performed. In the first, a 200 Ωm half-space is used to generate the sensitivities. In the second, the 1 Hz data were first inverted to recover a 3-D resistivity model.

The resulting chargeability model obtained by using sensitivities from a 200 Ωm half-space are shown in Fig. 8. A chargeable body is clearly recovered but the resolution is substantially reduced compared to that in Fig. 7. The body has moved towards the surface and it is also spread out in the horizontal direction. Nevertheless, the result provides useful information as its maximum value coincides horizontally with the centre of the true prism. This is a positive result and shows that knowledge of the background is important but not critical to getting some valuable information from the ISIP data. Moreover, the example given here (where the true resistivity in the model varies between 1 and 10 000 Ωm , and it has been replaced by a uniform Earth of 200 Ωm) is indicative of a very poor estimate of the resistivity.

In the second example, the contaminated 1Hz data were first inverted using the FEM inversion code EH3D (Haber *et al.* 2004) to recover a real 3-D resistivity model. Plan view and cross-sections of the true and recovered resistivity model are shown in Fig. 9. As the inversion is working with only a single frequency, the resulting resistivity model differs substantially from the true model. Most of the major features can be recognized in the result, but they are highly distorted.

The inversion of the ISIP data using the recovered conductivities are shown in Fig. 10. The chargeable block is now well recovered and is nearly the same as that obtained from using the true conductivity. There is however a small artefact at $(x, z) = (400, 400)$ which appears to stem from additional structure in the recovered conductivity.

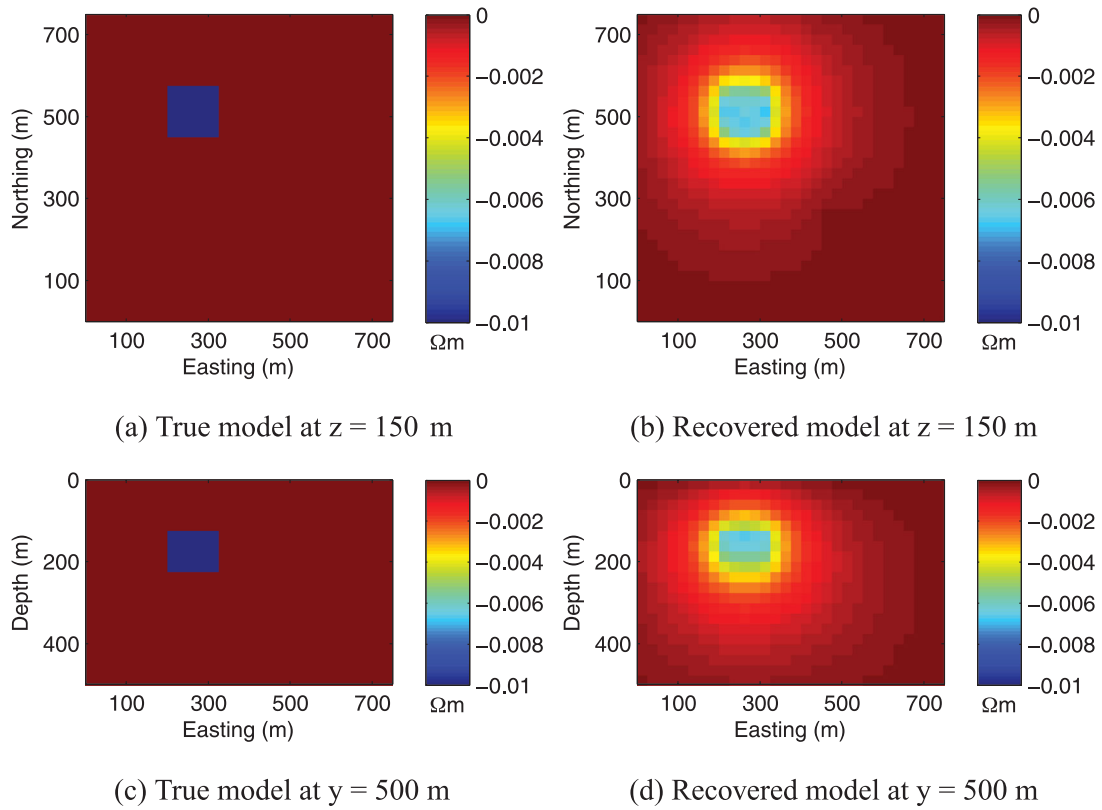


Figure 7. True and recovered $\delta\rho_{Re}$ models. The true zero-frequency resistivity model was used to generate sensitivities for the $\delta\rho_{Re}$ inversion.

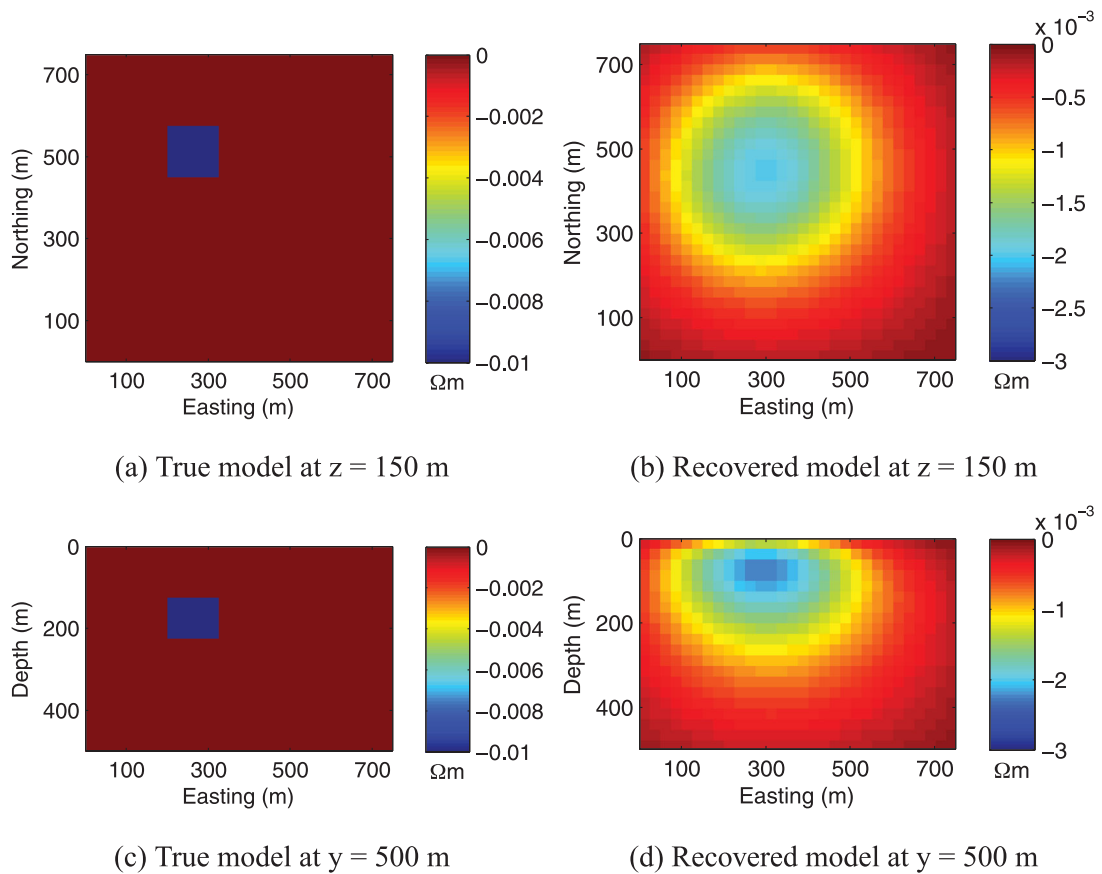


Figure 8. True and recovered $\delta\rho_{Re}$ models. A $200 \Omega\text{m}$ half-space resistivity model was used to generate sensitivities for the $\delta\rho_{Re}$ inversion.

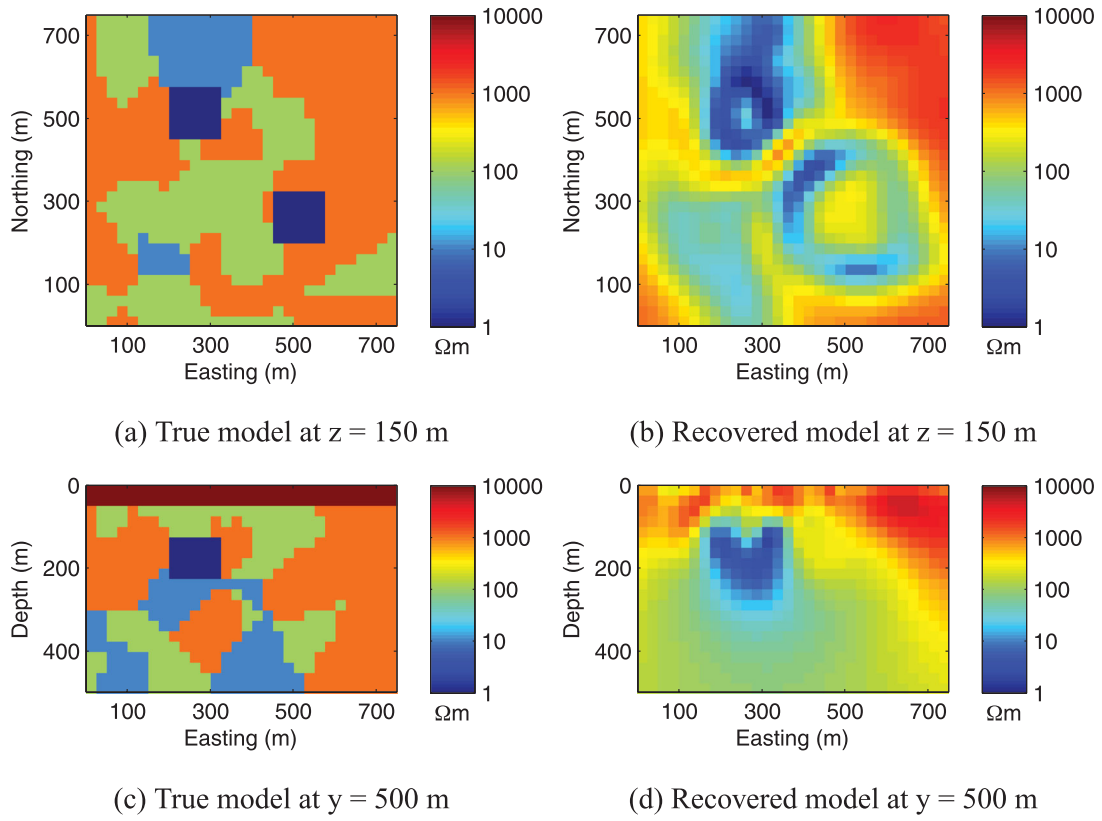


Figure 9. True and recovered resistivity models. Recovered models were produced by inverting the 1 Hz FEM data.

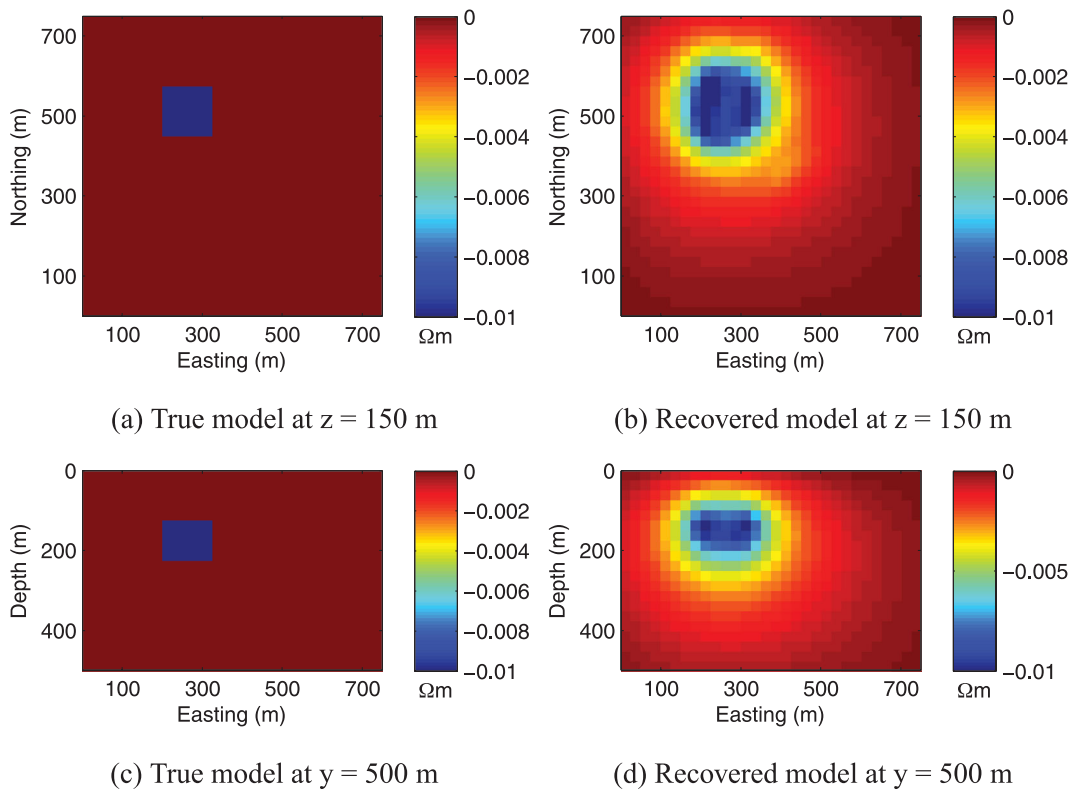


Figure 10. True and recovered $\delta\rho_{Re}$ models. The best fitting resistivity model to was used to generate sensitivities for the $\delta\rho_{Re}$ inversion.

6 CONCLUSIONS

In this paper, we have introduced a new methodology to invert for chargeability using inductive magnetic sources. Using the simple asymptotic behaviour of the fields at low frequencies we introduce new data, that we refer to as the ISIP data. At low frequencies these data are identically zero if the conductivity is purely real. Thus any non-zero value of this datum is a direct indicator of chargeable material. Numerical simulations demonstrate that this is true even in a complex geological environment.

We then develop a linearised approximation that relates ISIP data to the chargeability. The link between these two quantities is the sensitivity matrix, which is evaluated using the real, frequency independent, conductivity. In synthetic inversions we show that important information about the existence and location of the chargeable structure can be obtained even with a fairly poor knowledge about the conductivity and that the resolution increases as the quality of the conductivity model increases.

Our technique provides a new methodology for detecting and mapping the presence of chargeable material without needing to inject current into the ground or place electrodes to measure potentials. By avoiding these requirements our technique may prove to be a useful tool in geological settings where traditional IP difficult is difficult to perform.

ACKNOWLEDGMENTS

This research was supported by the Natural Sciences and Engineering Research Council of Canada and by the University of British Columbia. We would like to thank the Associate Editor, Oliver Ritter, as well as the reviewers, Andreas Hordt and James Macnae, for their constructive comments and reviews.

REFERENCES

- Amestoy, P.R., Guermouche, A., L'Excellent, J.Y. & Pralet, S., 2006. Hybrid scheduling for the parallel solution of linear systems, *Parallel Comput.*, **32**, 136–156.
- Beard, D. & Zhou, Q., 1995. Method of skin effect correction and data quality verification for a multifrequency induction well logging instrument, U.S. Patent 5 666 057.
- Chen, J. & Oldenburg, D.W., 2006. 3D inversion of magnetic induced polarization data. *Exploration Geophysics*, **37**, 245–253.
- Cole, K.S. & Cole, R.H., 1941. Dispersion and absorption in dielectrics, *J. Chem. Phys.*, **9**, 341–351.
- Davydycheva, S., Rykhlin, N. & Legeido, P., 2006. Electrical-prospecting method for hydrocarbon search using the induced-polarization effect, *Geophysics*, **71**, G179–G189.
- Fink, J.B., McAlister, E.O., Sternberg, B.K., Wieduwilt, W.G. & Ward, S.H., 1990. *Induced Polarization, Applications and Case Histories*, Vol. 4: Investigations in Geophysics, Society of Exploration Geophysicists, Tulsa, Oklahoma.
- Gasperikova, E. & Morrison, H.F., 2001. Mapping of induced polarization using natural fields, *Geophysics*, **66**, 137–147.
- Haber, E. & Ascher, U.M., 2001. Fast finite volume simulation of 3d electromagnetic problems with highly discontinuous coefficients, *SIAM J. Sci. Comput.*, **22**, 1216–1228.
- Haber, E., Oldenburg, D. & Ascher, U.M., 2004. Inversion of 3d electromagnetic data in frequency and time domain using an inexact all-at-once approach, *Geophysics*, **69**, 1216–1228.
- Hoheisel, A., Hördt, A. & Hanstein, T., 2004. The influence of induced polarization on long-offset transient electromagnetic data, *Geophys. Prospect.*, **52**, 417–426.
- Hohmann, G.W., Kintzinger, P.R., Van Voorhis, G.D. & Ward, S.H., 1970. Evaluation of the measurement of induced electrical polarization with an inductive system, *Geophysics*, **35**, 901–915.
- Hördt, A., Blasschek, R. & Kemna, A., 2007. Hydraulic conductivity estimation from induced polarisation data at the field scale—the Krauthausen case history, *J. appl. Geophys.*, **62**, 33–46.
- Kawai, J., Uehara, G., Kohrin, T., Ogata, H. & Kado, H., 1999. Three axis SQUID magnetometer for low-frequency geophysical applications, *IEEE Trans. Magn.*, **35**, 3974–3976.
- Kelley, C.T., 1999. *Iterative Methods for Optimization*, Vol. 18, SIAM Frontiers in Applied Mathematics.
- Li, Y. & Oldenburg, D.W., 2000. 3-D inversion of induced polarization data, *Geophysics*, **65**, 1931–1945.
- Morrison, H.F., Phillips, R.J. & O'Brian, D.P., 1969. Quantitative interpretation of transient electromagnetic fields over a layered halfspace, *Geophys. Prospect.*, **17**, 82–101.
- Oldenburg, D.W. & Li, Y., 2005. Inversion for applied geophysics: a tutorial, in *Near-Surface Geophysics, SEG Investigations in Geophysics Series No. 13*, pp. 89–150, ed. Butler, D.K., Society of Exploration Geophysicists, Tulsa, Oklahoma.
- Oldenburg, D.W. & Li, Y., 1994. Inversion of induced polarization data, *Geophysics*, **59**, 1327–1341.
- Pelton, W.H., Ward, S.H., Hallof, P.G., Sill, W.R. & Nelson, P.H., 1978. Mineral discrimination and removal of inductive inductive coupling with multifrequency IP, *Geophysics*, **43**, 588–609.
- Seigel, H.O., 1959. Mathematical formulation and type curves for induced polarization, *Geophysics*, **24**(3), 547–565.
- Seigel, H.O., 1974. The magnetic induced polarization (MIP) method, *Geophysics*, **39**, 321–339.
- Seigel, H.O., Nabighian, M., Parasnis, D.S. & Vozoff, K., 2007. The early history of the induced polarization method, *Leading Edge*, **26**, 312–321.
- Slater, L.D. & Glaser, D.R., 2003. Controls on induced polarization in sandy unconsolidated sediments and application to aquifer characterization, *Geophysics*, **68**, 1547–1558.
- Smith, R.S. & West, G.F., 1988. Inductive interaction between polarizable conductors: an explanation of a negative coincident-loop transient electromagnetic response, *Geophysics*, **53**, 677–690.
- Veeken, P.C.H., Kudryavceva, E.O., Putikov, O.F., Legeido, P.Y. & Ivanov, S.A., 2012. Modelling induced polarization effects due to pyrite in geochemical alteration zones above hydrocarbon accumulations, *Petrol. Geosci.*, **18**, 59–72.
- Wang, T., Yu, L. & Fanini, O., 2003. Multicomponent induction response in a borehole environment, *Geophysics*, **68**, 1510–1518.
- Weidelt, P., 1982. Response characteristics of coincident loop transient electromagnetic systems, *Geophysics*, **47**, 1325–1330.
- Wong, J., 1979. An electrochemical model of the induced-polarization phenomenon in disseminated sulfide ores, *Geophysics*, **44**, 1245–1265.
- Yee, K.S., 1966. Numerical solution of initial boundary value problems involving Maxwell's equations in isotropic media, *IEEE Trans. Antennas Propag.*, **14**, 302–307.